RSC Advances

PAPER

View Article Online
View Journal | View Issue

Cite this: *RSC Adv.*, 2025, **15**, 34976

Facile room-temperature solution-phase synthesis of a ZIF-67 : Ni hybrid-MOF battery type material for supercapacitor applications

Ndeye Fatou Diop,[a] Kabir Opeyemi Otun,[a] Souleymane Thior,[a] Vusani Muswa Maphiri,[a] Vianney Ngoyi Kitenge,[a] Samba Sarr,[a] Ndeye Fatou Sylla,[a] Xiang Wenqiang,[c] Mohamed Chaker,[c] Balla Diop Ngom[b] and Ncholu Manyala *[a]

Metal–organic frameworks (MOFs) have gained significant attention as potential supercapacitor electrodes due to their high surface area, tunability, and well-defined porosity. However, their application is often limited by low capacity, poor electrical conductivity, and weak substrate adhesion, as observed in zeolitic imidazolate framework-67 (ZIF-67). To address these limitations, this study investigates the effect of nickel incorporation into ZIF-67, aiming to enhance its electrochemical performance. A series of hybrid-MOFs, denoted as ZIF-67 : Ni (1 : *X*), were synthesized *via* a simple solution-phase method at room temperature by varying the nickel content. Nickel was introduced to facilitate faster redox reactions and improve ion transport, thereby enhancing charge storage capability. The optimized ZIF-67 : Ni (1 : 2) electrode exhibited a high specific capacity of 161.2 mA h g^{-1} at 1 A g^{-1}, with a capacity retention of 74.6% after 5000 charge–discharge cycles, outperforming pristine ZIF-67 and other nickel-mixture variants. The improved electrochemical performance is attributed to the enhanced porous structure, which increased active site accessibility and reduced charge transfer resistance. Furthermore, an asymmetric supercapacitor device assembled using ZIF-67 : Ni (1 : 2) as the positive electrode and activated carbon (AC) as the negative electrode (ZIF-67 : Ni (1 : 2)//AC) demonstrated a cell capacity of 44.6 mA h g^{-1}, a specific energy of 36.97 W h kg^{-1}, and a specific power of 416.3 W kg^{-1} at 0.5 A g^{-1}. Notably, the device exhibited excellent cycling stability, retaining 99.8% of its capacity after 10 000 cycles at 10 A g^{-1}. These findings highlight the potential of multi-metallic interactions in enhancing the electrochemical performance of ZIF-67-based MOFs, offering valuable insights for the development of high-performance supercapacitor electrodes.

Received 6th August 2025
Accepted 11th September 2025

DOI: 10.1039/d5ra05741h

rsc.li/rsc-advances

1. Introduction

High energy demand, combined with the rapid depletion of fossil fuels and the growing problem of environmental pollution, has influenced the development of alternative energy sources such as wind, solar, tidal and hydro energy.[1–3] However, due to the intermittent nature of these energy sources, they cannot produce energy continuously. Energy storage devices, such as supercapacitors and batteries, enable the storage of energy produced by these renewable sources, thereby bridging the production gap.[4] Supercapacitors (SCs) and batteries are the most promising energy storage systems because of their intriguing features, including high efficiency and durability. When compared to batteries, supercapacitors are advantageous due to their high specific capacitance, high specific power, long life cycle and quick charging and discharging. They function on the principle of electrostatic charge separation, redox reactions or both, unlike ordinary batteries that rely on chemical reactions to store energy. Based on their charge storage chemistry, supercapacitors can be classified into electric double-layer capacitors (EDLCs) and pseudocapacitors. EDLCs store charges electrostatically by absorbing ions on the surface of the electrode, while pseudocapacitors store energy electrochemically by rapid surface-controlled redox reactions. Hybrid supercapacitors combine capacitive and faradaic mechanisms to deliver high capacity together with impressive specific energy and specific power.[5–8]

Electrode materials and electrolytes determine the performance of supercapacitors (SCs). Selecting electrode materials with improved electrochemically active sites and chemical stability is therefore crucial. A wide range of materials,

[a]*Department of Physics, SARChI in Nano Materials for Energy Storage and Water Purification Applications, University of Pretoria, 0028, South Africa. E-mail: ncholu.manyala@up.ac.za; Tel: +27 12 420 3549*

[b]*Laboratoire de Photonique Quantique, d'Energie et de Nano-Fabrication, Faculté des Sciences et Techniques, Université Cheikh Anta Diop de Dakar (UCAD), B.P. 5005, Dakar-Fann Dakar, Senegal*

[c]*Institut National de la Recherche Scientifique Centre-Energie Matériaux Telecommunications, 1650, Boulevard Lionnel Boulet, Varennes, QC J3X 1S2, Canada*

including carbonaceous compounds such as graphene,[9,10] nanocarbon, activated carbon, and carbon nanotubes[11–13] as well as transition metal oxides[7,14] and conducting polymers, have been employed as electrodes in SCs.[15] However, their chemical and physical limitations impede their wide range of performance, which requires shifting attention towards other novel materials.

Metal–organic frameworks (MOFs) have received widespread attention lately as electrode materials for SCs owing to their flexible structural architecture and remarkable and adjustable chemical bonds between the metal and ligands. MOFs are classified as crystalline hybrid materials formed by the assemblage of inorganic metal ions (Ni,[16] Co,[16] Ce,[17] Zn,[18] Fe,[18] Mn,[19] *etc.*) and organic ligands (benzene-1,3,5-tricarboxylic acid (BTC),[20] 2-methylimidazole (2-mim),[21] 2,6-dinaphthalene dicarboxylic acid[17] and others). They are unique for their large specific surface areas, rich redox metal centres, high porosity and tuneable pore characteristics.[22–25] The most studied MOF for energy storage is cobalt-based MOF, denoted as ZIF-67 MOF. Due to its stability and ability to effectively transfer redox species between Co(II) and Co(III), cobalt is frequently chosen as one of the most preferred metal sources in the design of MOFs for energy storage applications.[26] However, ZIF-67 MOF, which is a single metal MOF, often exhibits good electrochemical performance but low-rate capability due to its limited conductivity. This leads to low electrical conductivity and poor stability, hindering its application in energy storage, including supercapacitors. To overcome this issue, the strategy is to incorporate a metal into the ZIF-67 structure to obtain hybrid-MOFs. This hybridization strategy seeks to combine the well-defined, porous morphology of ZIF-67 with the high redox activity and conductivity of nickel, thereby facilitating ion diffusion, charge-transfer kinetics, and electrolyte ion adsorption for distinctly improved electrical performance.[27–30] The reversible Ni^{2+}/Ni^{3+} redox couple of Ni makes it an ideal candidate for hybridization with ZIF-67, imparting significant pseudocapacitance to the resulting composite. Although pristine ZIF-67 offers exceptional porosity, its poor intrinsic conductivity limits its electrochemical utility. Incorporating nickel into the framework overcomes this drawback, delivering markedly improved capacitance, rate capability, and cycling stability.[30,31] For instance, Wu *et al.* synthesized a NiCo-LDH-S/PNT electrode material by preparing sulfur-doped NiCo-LDH on polypyrrole nanotubes (PNT) using ZIF-67 as a template through combined electrospinning and hydrothermal methods. Varying sulfur contents revealed hollow PPy (polypyrrole) tubes decorated with high-aspect-ratio NiCo-LDH-S sheets, which created charge-transfer pathways and extensive electrolyte contact, achieving a specific capacitance of 322.8 mA h g^{-1} at 10 mV s^{-1} with 7 wt% sulfur. NiCo-LDH-S/PNTs@NF at 1.3 V delivered an energy density of 16.28 W h kg^{-1} at 1 A g^{-1} and a power density of 650 W kg^{-1} and the CF retention of 74% and coulombic efficiency of 90% after 8000 cycles.[32] Rahim *et al.* synthesized a NiCo-ZIF bimetallic sample prepared by the co-precipitation method using 2-methylimidazole as a ligand. The metals were dissolved in distilled water, subsequently poured into a 2-methylimidazole solution and stirred magnetically. The NiCo-ZIF MOF, with cuboid rod-like shapes, exhibits a specific capacity of 99.44 mA h g^{-1} at a current density of 0.5 A g^{-1}. An asymmetric cell Ni/Co-ZIF//KOH//AC achieved an energy and power density of 16 W h kg^{-1} and 457 W kg^{-1}, respectively, tested in 1 M KOH.[33]

Despite these advances, most Ni/Co-MOF and NiCo-LDH electrodes reported to date rely on solvothermal, hydrothermal, or electrodeposition methods conducted at high temperatures and pressures. Furthermore, certain methods require the use of additional chemicals, which could present environmental hazards and incur significant costs.[30,34,35] In this work, a nickel-incorporated Co-MOF-based (ZIF-67) hybrid was designed and optimized using a facile room temperature (RT) solution-phase method. Due to its porous structure, increased electroactive surface area, and better storage capacity, the optimized hybrid-MOF (ZIF-67 : Ni (1 : 2)) was found to have a remarkable specific capacity of 161.2 mA h g^{-1} at 1 A g^{-1} and high cyclic stability (74.6% after 5000 cycles at 20 A g^{-1}) in the three-electrode evaluation. The device delivered a specific energy of 36.97 W h kg^{-1} and a power density of 416.3 W kg^{-1} at 0.5 A g^{-1}. The assembled asymmetric (ZIF-67 : Ni (1 : 2)//AC) device demonstrated an outstanding coulombic efficiency of 99.8% after 10 000 charge–discharge cycles at 10 A g^{-1}. Thus, this environmentally friendly approach for the synthesis of hybrid-MOFs is promising to enhance energy storage applications.

2. Experimental

2.1 Materials

Cobalt nitrate hexahydrate ($Co(NO_3)_2 \cdot 6H_2O$), nickel nitrate hexahydrate ($Ni(NO_3)_2 \cdot 6H_2O$), 2-methylimidazole ($C_4H_6N_2$), methanol (CH_3OH), ethanol (C_2H_5OH), potassium hydroxide (KOH, 99%), polyvinylidene fluoride (PVDF), carbon acetylene black (CAB), and *N*-methyl-2-pyrrolidone (NMP) were supplied by LABCHEM (Johannesburg, South Africa). Polycrystalline nickel foam mesh (with 1.6 mm thickness and 420 g m^{-2} areal density) was obtained from Alantum (Munich, Germany).

2.2. Synthesis of ZIF-67

ZIF-67 was synthesized *via* a modified, facile solution-phase method at room temperature. Initially, 2 mmol of cobalt nitrate hexahydrate ($Co(NO_3)_2 \cdot 6H_2O$) and 12 mmol of 2-methylimidazole ($C_4H_6N_2$) were separately dissolved in 30 mL and 10 mL of methanol, respectively, and stirred at room temperature. The $Co(NO_3)_2 \cdot 6H_2O$ solution was then slowly added to the 2-methylimidazole solution under continuous stirring, and the mixture was stirred for 24 hours. Methanol facilitates the rapid formation of ZIF-67 nuclei, accelerating crystal growth.[36] The resulting purple solution was centrifuged at 10 000 rpm for 10 minutes, and the precipitate was washed with ethanol and deionized water. Finally, the product was dried in a vacuum oven at 60 °C for 12 hours to obtain ZIF-67.

2.3 Synthesis of ZIF-67 : Ni

The ZIF-67 : Ni composite was synthesized using the following procedure: three separate portions of 0.2 g of the as-prepared ZIF-67 were each dispersed in 50 mL of ethanol. To these, 0.2 g, 0.4 g, and 0.8 g of Ni $(NO_3)_2 \cdot 6H_2O$ were individually added, corresponding to ZIF-67 : Ni ratios of 1 : 1, 1 : 2, and 1 : 4, respectively. The mixtures were stirred at room temperature for 1 hour and then left undisturbed for 12 hours at ambient temperature to facilitate crystallization. The resulting products were collected by centrifugation, washed, and dried under vacuum at 60 °C for 8 hours. The final composites ZIF-67 : Ni (1 : 1, 1 : 2, and 1 : 4) were obtained as illustrated in Scheme 1.

2.4. Physical characterization

The Raman spectroscopy of the hybrid-MOFs was determined using a WITec confocal Raman microscope (WITec Alpha 300 RAS+) with a 532 nm laser wavelength. X-Ray diffraction (XRD) analysis of ZIF-67 : Ni (1 : *X*), where *X* corresponds to the different mass ratios of Ni in ZIF-67 as 1, 2 and 4, and ZIF-67 samples was conducted using Bruker BV 2D phaser Cu-Kα (λ = 0.154 nm) radiation operating in the two-theta scan range of 5 to 80 degrees. To identify the functional groups, an FTIR spectrometer (FT/IR-6700, JASCO Corporation) was used with a wavenumber set from 400 to 4000 cm^{-1}. The surface morphologies of the synthesized materials and the EDX mapping image (Oxford 2.0) were investigated through a Zeiss Ultra Plus 55 field emission scanning electron microscopy (FE-SEM) powered at 2.0 kV. X-ray photoelectron spectroscopy (XPS) spectra were collected on a VG Escalab 220i-XL instrument equipped with a monochromatic Al-Kα excited energy source (0.6 eV). The specific surface area was determined by nitrogen adsorption–desorption measurements, and pore characteristics were obtained using the density functional theory (DFT) method on a NOVA-touch LX^2 system in a relative pressure (P/P_0) range of 0.05 to 0.95 at 77 K.

2.5. Electrochemical characterization

The nickel foam was thoroughly pre-treated by sequentially immersing it in 3 M HCl, acetone, and then absolute ethanol, each for 15 minutes. Finally, it was rinsed extensively with deionized water to ensure complete cleanliness. The cleaned nickel foam was dried at 60 °C overnight. This treatment eliminated the hydroxide layer and the inert oxide on the nickel metal surface, which occurs in a humid environment. The electrode materials comprising ZIF-67 : Ni (1 : *X*) active material, polyvinyl fluoride (PVDF as a binder) and acetylene carbon black (ACB) were prepared by mixing at a wt% of 80, 10, 10, respectively. A few drops of *N*-methyl-2-pyrrolidone (NMP) were added to the mixture in an agate mortar and mixed uniformly to make a slurry. The slurry was coated on the surface of a 1 cm × 1 cm clean nickel foam with a mass of the electrode material of about 2 mg cm^{-2} for each tested material and dried in an oven at 60 °C overnight. Nickel foam was selected as the substrate for all electrochemical measurements due to its unique combination of high electrical conductivity and excellent chemical stability in alkaline electrolytes. These properties make nickel foam a widely used and well-accepted current collector for electrochemical measurements, including battery-type and pseudocapacitive electrode materials. In contrast, alternatives, such as copper foam or aluminium foam, are less stable in alkaline media, while graphite substrates typically offer lower conductivity and limited active surface area for electrochemical processes.[37,38]

To study the electrochemical performances of ZIF-67 and ZIF-67 : Ni (1 : *X*) electrodes, a three-electrode system configuration was employed, which consisted of a glassy carbon, Ag/AgCl (in saturated 3 M KCl (potassium chloride)) and the synthesized materials as the counter, reference and working electrodes, respectively. The measurements were carried out in a 6 M KOH electrolyte, which was found to be the best-performing electrolyte for the materials. The electrochemical

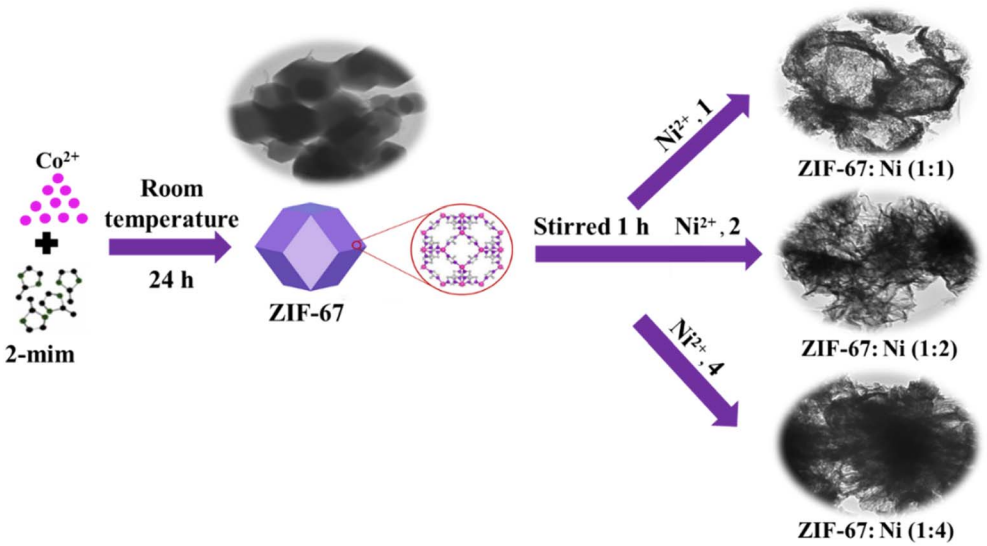

Scheme 1 Illustration of the synthesis of dodecahedron ZIF-67 and Ni/Co hybrid-MOFs at different Ni ratios.

data were obtained from a Bio-Logic VMP-300 16-channel potentiostat (Knoxville, USA) at ambient temperature, and were used to evaluate parameters like specific capacity, cyclic stability, specific energy and power. The cyclic voltammetry (CV) curves were evaluated at different scan rates (in mV s^{-1}) from 2 to 100, and the galvanostatic charge–discharge (GCD) plots were obtained by varying the specific current (in A g^{-1}) from 1 to 20 with a potential window ranging from 0 to 0.55 V. The specific capacity, Q_s (mA h g^{-1}), was calculated from the discharge of the GCD curves using eqn (1), leveraging their pronounced faradaic behaviour. This characteristic enables precise integration of current over time, signifying true electrochemical energy storage through reversible redox reactions rather than simple electrostatic charge accumulation.[5] Electrochemical impedance spectroscopy (EIS) measurements were tested with a frequency range of 100 kHz to 10 mHz.

$$Q_s = \frac{I \times \Delta t}{3.6 \times m} \quad (1)$$

where I represents the current (mA), Δt (s) is the discharge time and m (g) is the mass of the electrode.

For the full-cell (two-electrode) measurement, a split-cell and a microfiber filter paper as a separator were used to assemble the asymmetric device in the same electrolyte (6 M KOH) using the ZIF-67 : Ni (1 : X) hybrid-MOF and activated carbon as positive and negative electrodes, respectively. The balancing of charges was estimated using eqn (2) below:

$$\frac{m_+}{m_-} = \frac{C_{s-} \times \Delta V_-}{3.6 \times Q_{s+}} \quad (2)$$

Q_{s+} is the specific capacity (mA h g^{-1}) of the positive electrode, C_- is the specific capacitance (F g^{-1}), ΔV_- is the potential window of the negative electrode, and m_+/m_- are the masses of the positive (+) and negative (−) electrodes in mg. The total mass used for the device is 4.5 mg. In addition, the specific energy E_s (W h kg^{-1}) of the asymmetric supercapacitor (ASC) device was obtained by evaluating the area under the discharge curve (GCD) as in eqn (3) and the specific power P_s (W kg^{-1}) was calculated using eqn (4), which is similar to eqn (1) used for the calculation of specific capacity, but with m being the total mass of both positive and negative electrodes:

$$E_s = \frac{I}{3.6 \times m} \int V \mathrm{d}t \quad (3)$$

$$P_s = \frac{3600 \times E_s}{\Delta t} \quad (4)$$

where I refers to the discharge current (A), m is the total mass of active materials (g), V represents the operating cell voltage (V) and t is the electrode discharge time (s).

3. Results and discussion

3.1 Structural, textural and morphological characterizations

The Raman spectra of the synthesized materials are presented in Fig. 1(a). Characteristic vibrational modes are observed at 124.28 cm^{-1}, 170.87 cm^{-1}, 257.16 cm^{-1}, 308.16 cm^{-1}, 423.22 cm^{-1}, and 1139 cm^{-1}, consistent with the previously reported values for ZIF-67.[39,40] The incorporation of nickel ions into the ZIF-67 MOF matrix yields a distinct Ni–O band at 514 cm^{-1} in the ZIF-67 : Ni (1 : 1), ZIF-67 : Ni (1 : 2), and ZIF-67 : Ni (1 : 4) composites. Moreover, a Co–O band at 477 cm^{-1} is also detected in all synthesized samples.[7,35,39,41,42] The absence of ZIF-67 pristine bands in the composites suggests significant restructuring of the ligand matrix. This is caused by the deprotonation of 2-methylimidazole, which coordinates to the nickel metal centre.[43,44] These findings confirm the successful incorporation of nickel within the ZIF-67 MOF matrix, resulting in the formation of the desired hybrid-MOF. The crystal structures of the four obtained materials were patterned by XRD analysis. Fig. 1(b) shows characteristic 2θ peaks at 8.2°, 12.3°, 14.7°, 17.07°, 19.08°, 22.7°, and 25.2°, corresponding to the (011), (112), (022), (013), (114), (223), and (224) crystal planes, respectively. These diffraction peaks are consistent with the characteristic crystalline pattern of ZIF-67, as previously reported in the literature.[45–47] Upon incorporating varying amounts of the nickel source, the resulting hybrid-MOF (ZIF-67 : Ni (1 : X)) exhibits broad peaks. It shows additional peaks at 39.7, 46.3, 54.9 and 70.9^0, corresponding to the (103), (018), (224), (024) and (220), crystalline planes, respectively, assigned to the planes of $Co(OH)_2$ (JCPDS no. 30-0443) and $Ni(OH)_2$ (JCPDS no. 14-0117), suggesting the formation of a NiO and CoO-related ZIF-67 hybrid mixed phase solid solution.[48] The peaks at around 12.3, 20.8, and 33.3^0, related to the (003), (006) and (101) planes, are shifted to the higher values due to Ni incorporation.[33,34,49] The crystal structure of ZIF-67 showed a distortion, indicating the presence of Ni, which suggests the successful synthesis of the ZIF-67 : Ni (1 : X) hybrid-MOF. The most intense diffraction peaks were fitted using a pseudo-Voigt profile and are displayed in Fig. S1, and the average crystallite size was estimated using the Scherrer equation,[50] as expressed below:

$$D = \frac{K\lambda}{\beta \cos \theta} \quad (5)$$

Here, D is the crystallite size (in nm), K is the shape factor (0.9), λ is the X-ray wavelength (Cu Kα = 1.5406 Å), β is the full width at half maximum (FWHM) of the fitted peak (in radians), and θ is the Bragg angle (in radians). ZIF-67 showed a crystallite size of 33 nm, while ZIF-67 : Ni (1 : 1), ZIF-67 : Ni (1 : 2), and ZIF-67 : Ni (1 : 4) showed the following values: 4.46 nm, 7.06 nm and, 4.87 nm, respectively. The ZIF-67 : Ni (1 : X) crystallite size has a standard deviation of 1.4 nm, suggesting that the increase in Ni content has an impact on the crystallite size, with ZIF-67 : Ni (1 : 2) having a larger crystallite size, which can form better-developed pores/cavities in the ZIF structure, leading to an increased accessible mesopores, improving electrode/electrolyte contact, and reduces resistance.[51]

The functional groups and bonding information of the prepared ZIF-67 and hybrid-MOF materials were investigated using FTIR spectroscopy, as shown in Fig. 1(c). The absorption peaks present at 1678, 1586, 1428, 1303, 1172, 1140, 985, 757, 698 and 431 cm^{-1} belong to the stretching and bending modes of ZIF-67.[52] As suggested in the Raman spectrum (Fig. 1(a)), these peaks seem to be unnoticed within the composites, likely

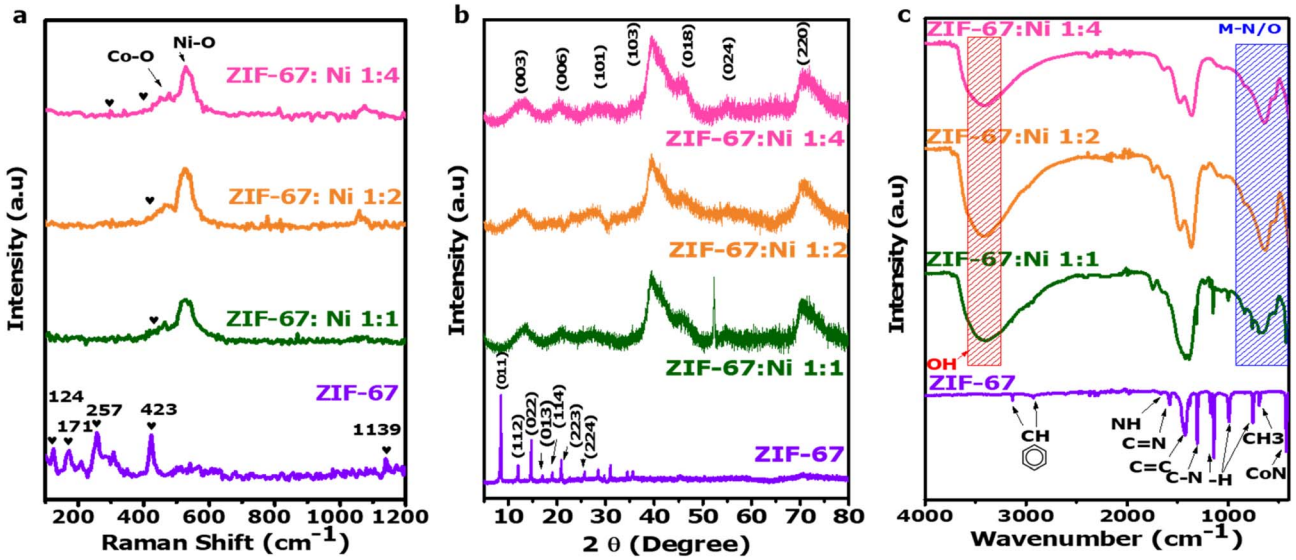

Fig. 1 (a) Raman spectra, (b) XRD patterns and (c) FTIR spectra of ZIF-67, ZIF-67 : Ni (1 : 1), ZIF-67 : Ni (1 : 2), and ZIF-67 : Ni (1 : 4).

due to the rearrangement of the ligand matrix. The ZIF-67 : Ni (1 : 1), ZIF-67 : Ni (1 : 2) and ZIF-67 : Ni (1 : 4) samples show broad peaks located at around 3300–3500 cm^{-1}, indicating the hydroxyl group of water molecules comprised within the samples.[53,54] Also, bending vibrations corresponding to the N-bond (1678 cm^{-1}) appears in all the hybrid-MOFs (ZIF-67 : Ni (1 : 1), ZIF-67 : Ni (1 : 2) and ZIF-67 : Ni (1 : 4)). The stretching vibrations of Ni–N and Ni–O are observed at 662 cm^{-1}, 663 cm^{-1}, and 665 cm^{-1} for ZIF-67 : Ni (1 : 1), ZIF-67 : Ni (1 : 2) and ZIF-67 : Ni (1 : 4), respectively. Furthermore, the Co–N peaks located at around 428 cm^{-1} and overlapping with the Co–O are consistently present across all synthesized samples.[33,35,43,54,55] These results conformed with the XRD and Raman spectra, suggesting that ZIF-67 and ZIF-67 : Ni hybrid-MOFs were successfully formed.

The morphology of the pristine and hybrid-MOF nanostructures was examined using field emission scanning electron microscopy (FESEM). ZIF-67 displays a rhombic dodecahedral structure, as shown in Fig. 2(a), accompanied by an inset histogram depicting particle size distribution. In contrast, incorporating Ni^{2+} into the ZIF-67 framework significantly alters the morphology, transitioning from well-defined rhombic dodecahedra to an irregular, nanograins-like morphology (Fig. 2(b)). The histogram inset in Fig. 2(b) shows the increase in the average particle size of ZIF-67 : Ni (1 : 2). This transformation suggests that Ni^{2+} plays a pivotal role in disrupting the original crystal growth pathway, possibly by coordinating differently with the organic ligands. These nanograins not only indicate a structural rearrangement but could also facilitate the accessibility of active sites, potentially benefiting electrochemical performance, as depicted in Fig. 2(b) and S2(a) and (b).[56]

The EDS elemental mapping of the ZIF-67 : Ni (1 : 2) sample, presented in Fig. 2(c), confirms the presence and uniform distribution of Co, Ni, C, N, and O throughout the structure. Similar elemental homogeneity was observed in the other composite samples. Additionally, EDS spectrum analysis was performed on both ZIF-67 and ZIF-67 : Ni (1 : *X*) variants, as detailed in Fig. S3 and Table 1. The results indicate that these materials are primarily composed of Co, Ni, O, and C. Although N is expected to be present due to its role in the organic linker structure of MOFs, its signal is notably weak in the EDS results. This can be attributed to the inherent limitations of EDS in detecting low atomic number elements like nitrogen, especially when present in small quantities or embedded within an organic matrix. Additionally, overlapping energy peaks with other elements and surface charging effects in non-conductive samples may further obscure its detection. Despite this, the structural presence of nitrogen is supported by complementary techniques, such as FTIR or elemental analysis, confirming its integration within the framework. The consistent distribution of Ni and Co elements suggests the effective incorporation of Ni into the Co-MOF framework *via* coordination with the organic ligand. The insets in Fig. S2 and the data in Table 1 provide the elemental weight percentages of the synthesized materials.

Upon immersion in an alkaline solution and introduction of Ni^{2+} for a period of time, we clearly noticed that the rhombic dodecahedral structure transformed into dense ultrathin as shown by TEM images (Fig. 2(d) and S2(c) and (d)). The ultrathin characteristics resulting from Ni incorporation are clearly depicted in the TEM images, further confirming the development of a wrinkled morphology. Notably, as the Ni concentration increases to the ZIF-67 : Ni (1 : 4) composition, particle agglomeration becomes more pronounced, as shown in Fig. S2(d). Additionally, the ZIF-67 : Ni (1 : 2) hybrid-MOF nanoparticles exhibit numerous voids, which could potentially enhance electrolyte diffusion and charge transport pathways.[57]

Considering the results and discussion above, the formation mechanism of ZIF-67 and ZIF-67 : Ni (1 : *X*) can be described

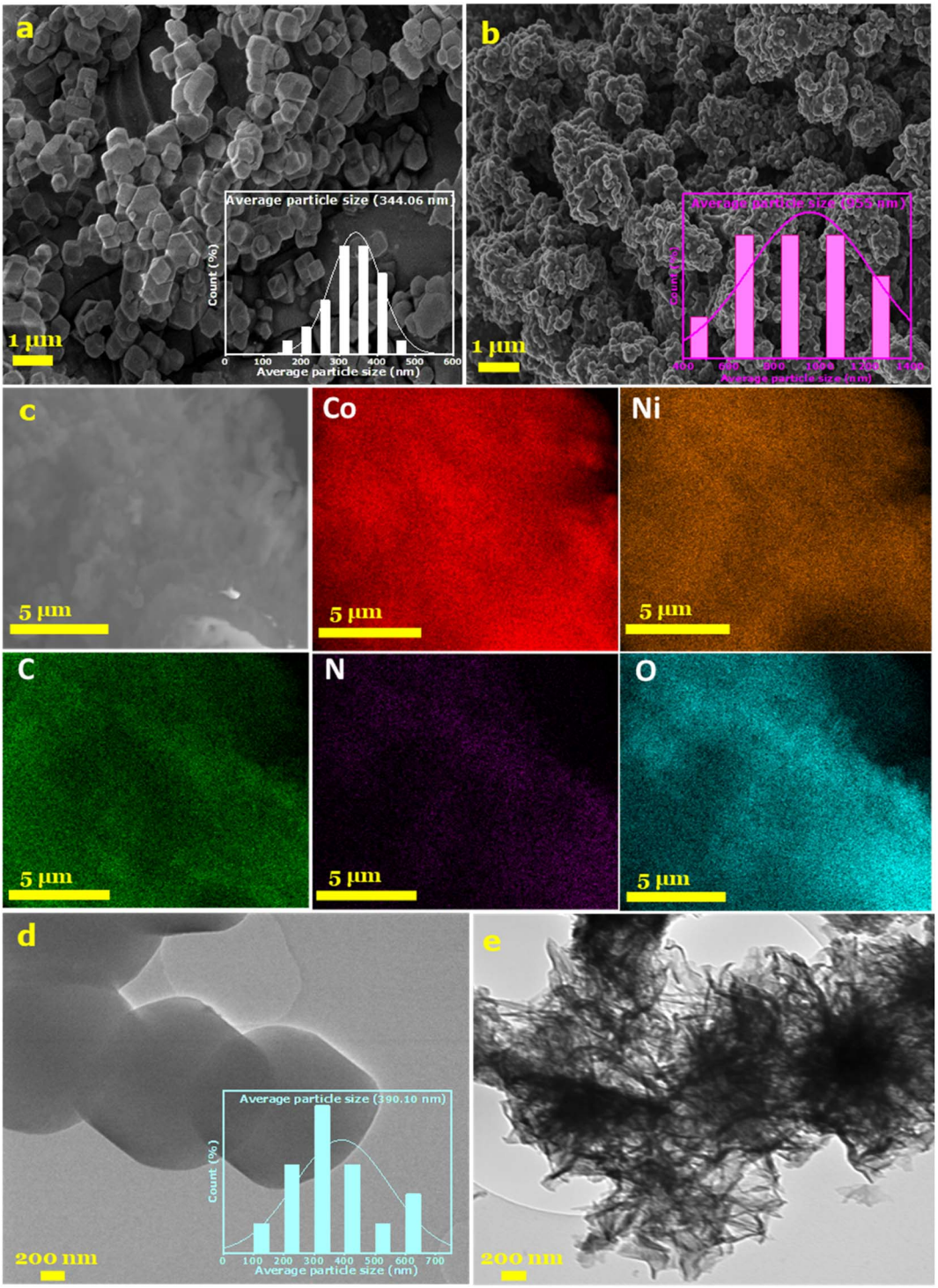

Fig. 2 SEM images at low magnification of (a) ZIF-67 and (b) ZIF-67 : Ni (1 : 2), TEM images of (c) ZIF-67 and (d) ZIF-67 : Ni (1 : 2) and (e) EDX mapping showing the elemental distribution of Co, Ni, C, N and O of ZIF-67 : Ni (1 : 2).

schematically, as shown in Fig. 3. The deprotonation and nucleation rates of 2-methylimidazole in methanol and ethanol facilitate the coordination of the 2-methylimidazole ligand with suitable cobalt and nickel ions.

To obtain a more comprehensive understanding of the composition of ZIF-67 : Ni $(1 : X)$, XPS was used to inspect the electronic state of the elements. Fig S4(a) shows the wide survey spectrum, which identifies the primary elements, as shown in Table 1. The high-resolution of Ni 2p in Fig. 4(a) exhibits four characteristic peaks, with two major peaks at 855.1 and 872.9 eV attributed to the $2p_{3/2}$ and $2p_{1/2}$, respectively. They are assigned to Ni–N and Ni–O. The coexistence of Ni–N and Ni–O

Table 1 Summary of elements and their corresponding EDS weight%

Elements	ZIF-67	ZIF-67 : Ni (1 : 1)	ZIF-67 : Ni (1 : 2)	ZIF-67 : Ni (1 : 4)
C	67.60	20.10	31.60	19.00
Co	16.40	39.30	25.50	30.70
O	11.60	27.80	15.10	14.30
N	4.40	—	—	—
Ni	0	12.80	28.10	35.70

coordination environments can lead to synergistic effects, enhancing the stability, conductivity and charge transfer properties of the material, which are crucial in electrochemical applications.[43,58] These peaks of Ni are accompanied by two deconvoluted peaks (Sat) at 861.2 and 879.1 eV. For the Co 2p spectrum (Fig. 4(b)), four peaks were identified showing the binding energy peaks at 780.7, 796.3, 785.2 and 801.8 eV, corresponding to $2p_{3/2}$, $2p_{1/2}$ and two satellites, respectively. These binding energies are characteristic of Co^{2+} species, indicating that cobalt exists predominantly in an oxidized state within the sample. Their intensity and position are strong indicators of the high-spin Co^{2+} configuration, commonly observed in cobalt oxides or cobalt–nitrogen coordination environments.[59,60] In Fig. 4(c), the fitted C 1s peaks at binding energies 284.4, 285.8 and 288.4 eV can be attributed to C–C/C=C, C=N and C–N from 2-methylamidazole, respectively.[61] The high magnification of O 1s display two peaks at binding energies of 530 eV and 532 eV, corresponding to the metal (Ni and Co) bonded to O and to hydroxyls ions, as shown in Fig. 4(d).[62] Fig. S4(b) shows the XPS spectrum of N 1s, and the peaks are located at binding energies around 398.6, 399.7, 400.1 and 401.5 eV, corresponding to the peaks of pyrrolic N, Co–N, Ni–N and graphitic N, respectively.[63–65] Overall, the XPS spectra results of ZIF-67 : Ni (1 : 2) MOF confirm the effective synthesis of ZIF-67 : Ni (1 : *X*) hybrid-MOFs. In addition, these data reveal that a high population of O and N could enhance electrical conductivity and supply more Ni and Co bonded to O and N active sites for electrochemical performances.[66]

The specific surface area (SSA) and pore size distribution (PSD) of the as-synthesized materials were further investigated by N_2 adsorption and desorption. The isotherms in Fig. 5(a) illustrate a typical type IV isotherm with H4-hysteresis loop, indicating the presence of slit-wedge shaped pores, which are typically associated with the MOF structure. These hysteresis loops also show the existence of a mesoporous structure.[67,68] Fig. 5(b) displays the distribution of pore size as determined by density functional theory (DFT) analysis, confirming the distribution of mesopores, which provide pathways for ion transport within the ZIF-67 : Ni (1 : *X*) samples.[13]

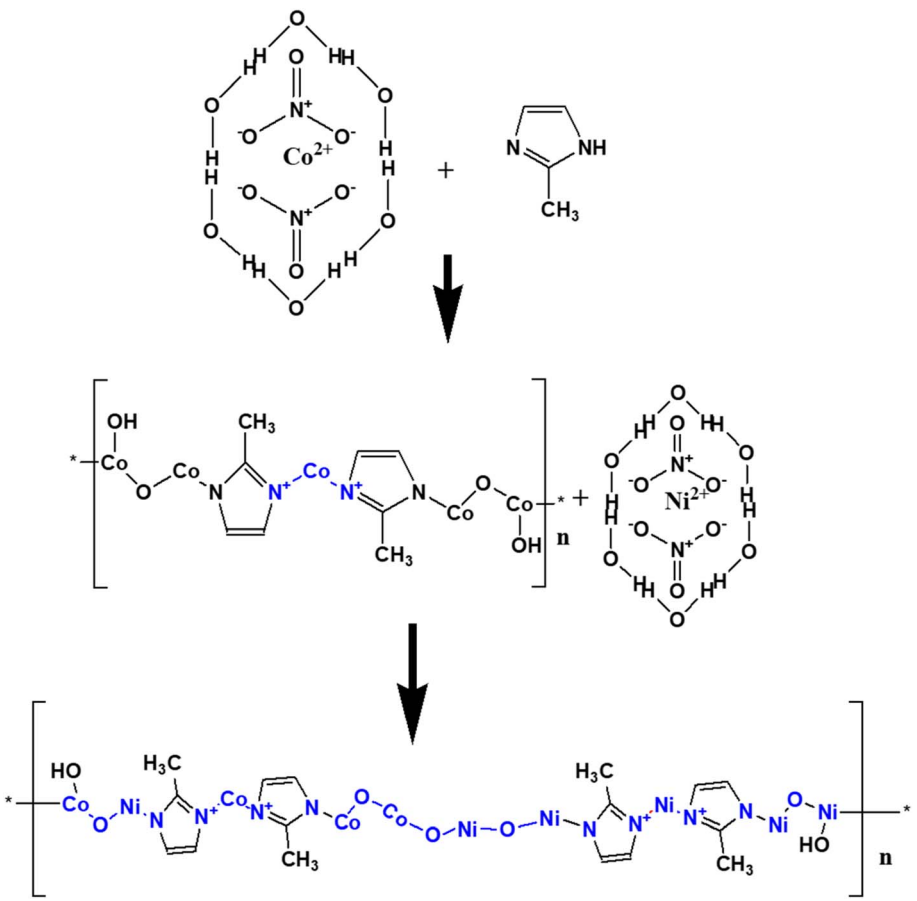

Fig. 3 Scheme illustrating the formation processes of ZIF-67 and ZIF-67 : Ni.

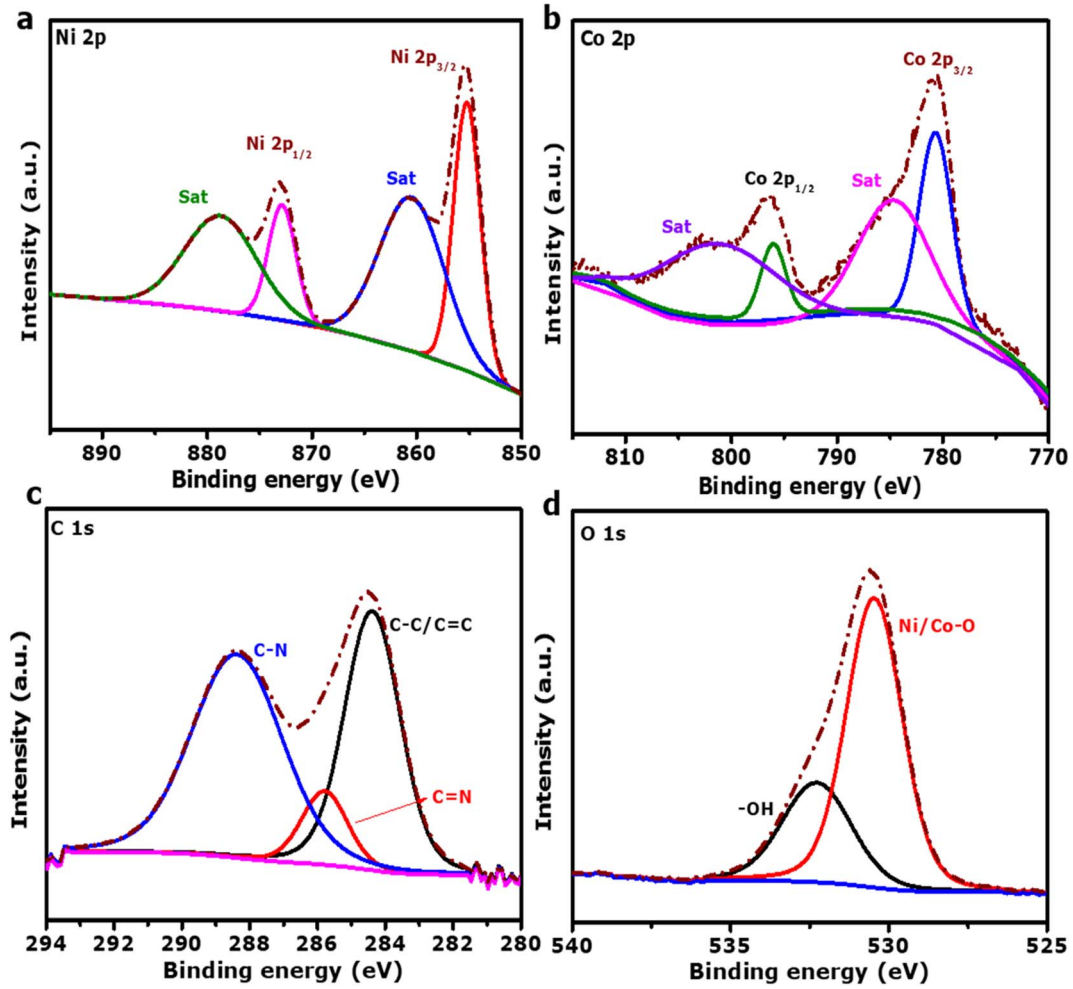

Fig. 4 (a) Deconvoluted XPS of Ni 2p, (b) Co 2p, (c) C 1s and (d) O 1s spectra of ZIF-67 : Ni (1 : 2).

The SSA of the ZIF-67 : Ni (1 : X) decreased due to the addition of Ni^{2+} ions in the pristine due to its bigger ionic radius as compared to Co^{2+}, which can be attributed to the larger ionic radius of Ni^{2+} (0.69 Å) compared to Co^{2+} (0.65 Å).[69] As a result, a reduction in SSA is observed, accompanied by an increase in both pore diameter and pore volume, as detailed in Table 2. This may enhance the contact area and expose more active sites between the electrode and the electrolyte, hence improving the

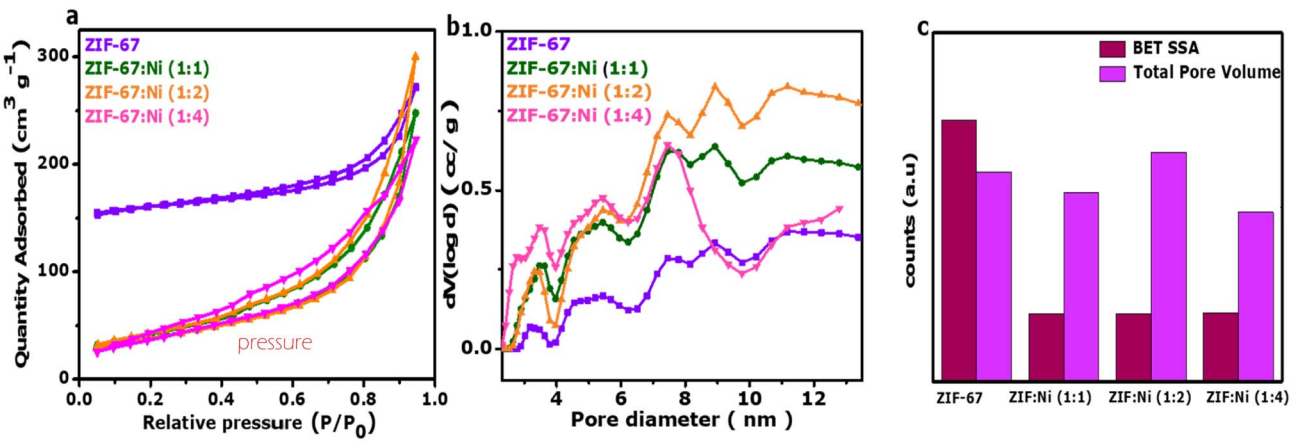

Fig. 5 (a) Nitrogen adsorption/desorption isotherms, (b) DFT pore size distribution curves and (c) histogram of ZIF-67, ZIF-67 : Ni (1 : 1), ZIF-67 : Ni (1 : 2), and ZIF-67 : Ni (1 : 4).

Table 2 Textural property data of ZIF-67 and ZIF-67 : Ni (1 : *X*) samples

Samples	BET SSA ($m^2\ g^{-1}$)	Mesopore SA ($m^2\ g^{-1}$)	Total pore volume ($cm^3\ g^{-1}$)	Volume meso ($cm^3\ g^{-1}$)	Pore diameter (nm)
ZIF-67	524.79	74.97	0.42	0.20	3.21
ZIF-67 : Ni (1 : 1)	135.64	135.48	0.38	0.32	11.33
ZIF-67 : Ni (1 : 2)	136.48	136.48	0.46	0.38	13.65
ZIF-67 : Ni (1 : 4)	137.23	137.23	0.34	0.34	10.55

electrochemical performance.[70] However, compared to other hybrid-MOFs, ZIF-67 : Ni (1 : 2) has the highest pore diameter and pore volume (Fig. 5(c)).[71] Furthermore, during the charge and discharge process, mesopores can quicken the movement and migration of electrolyte ions.[72,73]

3.2. Electrochemical characterization

3.2.1. Three-electrode configuration. The electrochemical properties of the ZIF-67 and ZIF-67 : Ni (1 : *X*) composites electrodes were analyzed using cyclic voltammetry (CV), galvanostatic charge–discharge (GCD) and electrochemical impedance spectroscopy (EIS) measurements. To evaluate how electrolyte properties impact supercapacitor behavior, the three electrodes were evaluated in various electrolytes, specifically potassium hydroxide (KOH) (1 M, 3 M, and 6 M), 1 M potassium nitrate (KNO_3) and 1 M sodium nitrate ($NaNO_3$), selected for their conductivity, stability, and compatibility with the synthesized electrodes. Among them, 6 M KOH exhibited the strongest current response and longest discharge time, indicating superior redox activity and charge capacity. Neutral electrolytes (KNO_3, $NaNO_3$) showed weaker performance, with low current response and shorter discharge times despite broader potential windows, as shown in Fig. S5(a) and (b). Ultimately, 6 M KOH was identified as the optimal electrolyte in a half-cell configuration, exhibiting the highest current response and longest discharge time and operating effectively within a 0.0–0.55 V potential window.[74]

As shown in Fig. 6(a), the CV curves of ZIF-67, ZIF-67 : Ni (1 : 1), ZIF-67 : Ni (1 : 2), and ZIF-67 : Ni (1 : 4) demonstrate faradaic behaviour. The hybrid-MOF nanocomposite electrode (ZIF-67 : Ni (1 : 2)) exhibits the largest current response as compared to other samples, leading to the highest specific capacity. CVs display well-defined anodic and cathodic peaks, confirming fast, reversible redox processes in the Ni-doped ZIF-67/Ni-foam electrodes. Peak currents and the anodic–cathodic separation vary with the Ni : ZIF-67 ratio, with a 1 : 2 sample showing the highest currents and the smallest ΔE_p, indicative of optimal charge-transfer kinetics and abundant active sites. They exhibited clear oxidation and reduction peaks, indicating reversible electrochemical reactions occurring in a redox reaction of the electrode materials. Fig. S6(a–d) presents the detailed CV curves of ZIF-67, ZIF-67 : Ni (1 : 1), ZIF-67 : Ni (1 : 2) and ZIF-67 : Ni (1 : 4) at a scan rate of 2–100 mV s^{-1} where all the samples maintain the faradaic behaviour. The anodic and cathodic peaks presented a right-shift and left-shift, respectively, with the increase in the scan rates. This implies that at a higher scan rate, there is greater restriction of ion transport and charge transfer kinetics between the active materials and electrolyte ions.[22,23,39] The GCD curves in Fig. 6(b) and S7 were used to calculate the specific capacity *via* eqn (1).

According to Fig. 6(c), the specific capacities of the as-prepared samples were calculated to be 51, 128, 161 and 143 mA h g^{-1} at a specific current of 1 A g^{-1}, respectively, for all samples, with ZIF-67 : Ni (1 : 2) showing the highest specific capacity throughout all specific currents used. The results confirmed the advantage of nickel incorporation for improving the electrochemical performance of the electrode materials. Rising current densities lead to a drop in specific capacity because ions cannot diffuse quickly through the pore network of the material.[34] Fig. 6(d) shows the Nyquist plots of ZIF-67, ZIF-67 : Ni (1 : 1), ZIF-67 : Ni (1 : 2) and ZIF-67 : Ni (1 : 4) samples. The intercept of the *x*-axis in the high frequency region indicates equivalent series resistance, and it is denoted as R_s. In comparison to ZIF-67 with $R_s = 0.31\ \Omega$, ZIF-67 : Ni (1 : 1), ZIF-67 : Ni (1 : 2), and ZIF-67 : Ni (1 : 4) have R_S values of 0.27 Ω, 0.29 Ω and 0.20 Ω, respectively. The charge transfer resistance, R_{ct}, was determined from the diameter of the semi-circle, which was found to be 0.23, 0.73, 0.03 and 1.32 Ω for ZIF-67, ZIF-67 : Ni (1 : 1), ZIF-67 : Ni (1 : 2) and ZIF-67 : Ni (1 : 4), respectively. From all these data, it is clear that ZIF-67 : Ni (1 : 2) recorded the lowest values for both R_s and R_{ct} and also the shortest diffusion length (15 Ω). At low frequencies, all samples showed a quasi-vertical shape referring to a faradaic behavior, but with ZIF-67 : Ni (1 : 2) having the shorter diffusion length, being closer to the *y*-axis, which may suggest a strong charge transport capability and imply better electrochemical performance.[75,76] To evaluate the stability of the materials, the electrodes were exposed to 5000 charge–discharge cycles. Fig. 6(e) shows the capacity retention as a function of the cycle number. The ZIF-67 : Ni (1 : 2) samples, as compared to ZIF-67 : Ni (1 : 1) and ZIF-67 : Ni (1 : 4) samples, have illustrated a very good capacity retention of 74.6% after 5000 cycles at 20 A g^{-1}.

3.2.2 Electrochemical kinetics analysis. A further electrochemical kinetics study was performed for ZIF-67 : Ni (1 : 2) because of its superior electrochemical performance as compared to the other samples. The power law (eqn (4)), which provides the relationship between the peak current of the CV curve and the scan rate, was employed for the study.[77]

$$i(V) = av^b \tag{6}$$

Here, $i(V)$ (A g^{-1}) represents the peak current, v (mV s^{-1}) is the scan rate, and a and *b* are the slope and intercept, respectively, of a linear plot ($\log i$ *versus* $\log v$) at 0.35 V.

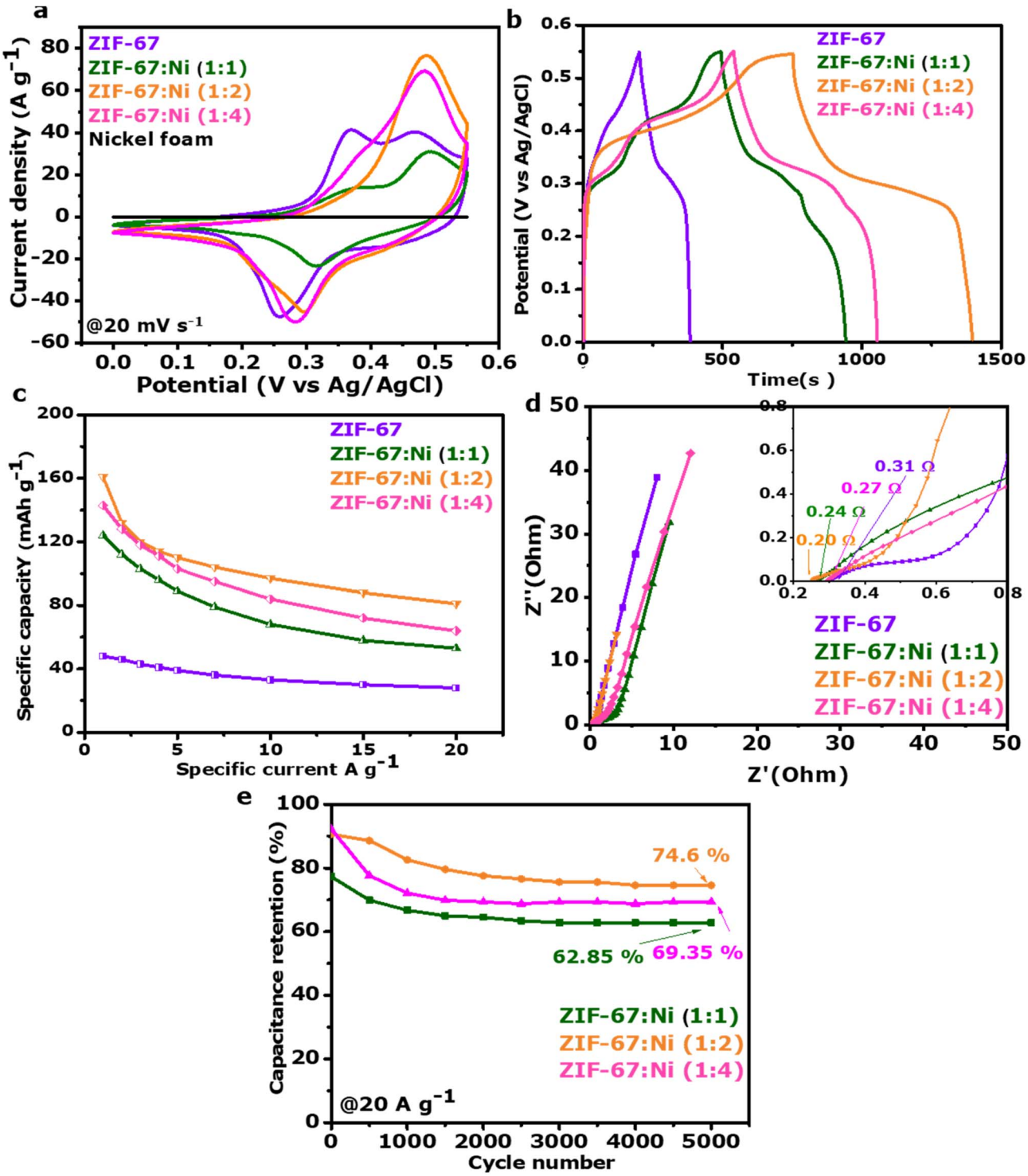

Fig. 6 (a) CV curves of the different electrodes at 20 mV s^{-1}, (b) GCD curves at of the different electrodes 1 A g^{-1}, (c) specific capacity against specific current of the different electrodes, (d) Nyquist plot of the different electrodes (inset shows the magnified plot) and (e) capacity retention of ZIF-67 : Ni (1 : *X*) up to 5000 cycles at a constant specific current at 20 A g^{-1}.

The linear plot of the anodic peaks (log *i vs.* log *v*) is displayed in Fig. 7(a). Generally, surface-controlled processes, such as EDLCs, contribute to capacitive behavior when the *b* value is close to 1. On the other hand, the *b* value near 0.5 indicates an optimal diffusion-controlled intercalation process, which is associated with faradaic materials.[78] Herein, the *b* value for ZIF-67 : Ni (1 : 2) was calculated to be 0.53, further implying that the ion transportation process is primarily diffusion-controlled behavior.

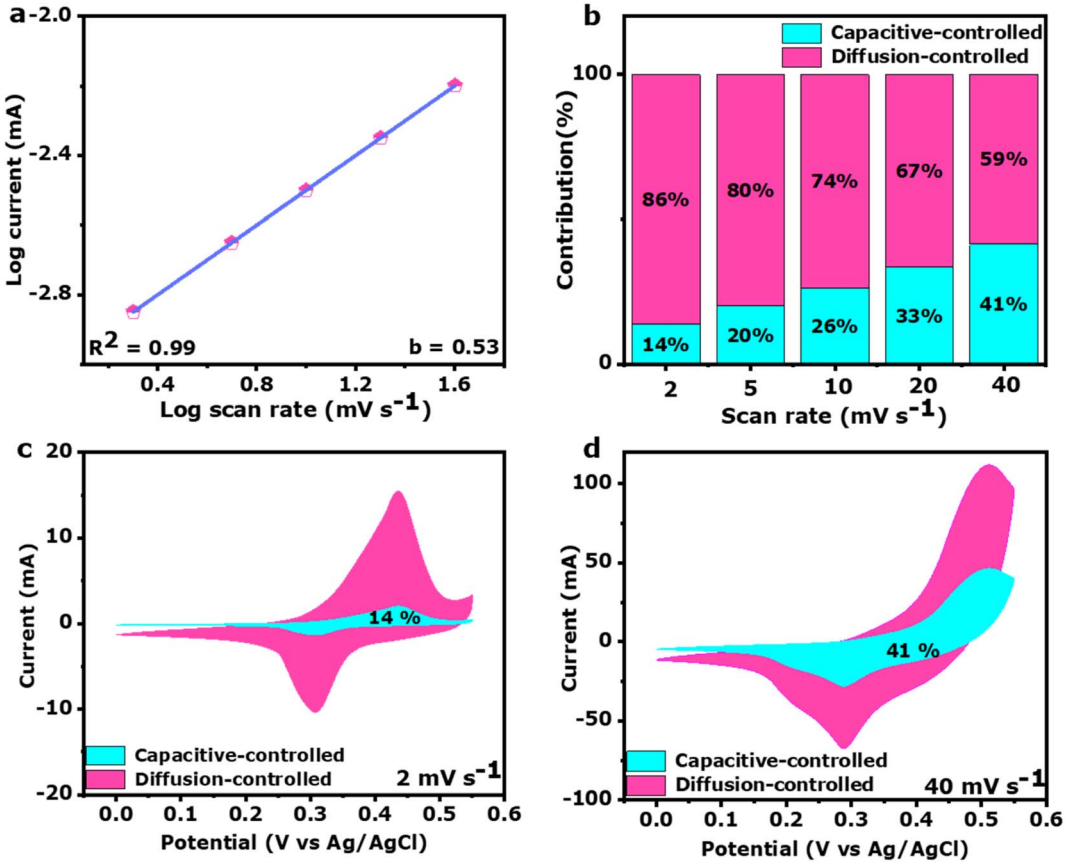

Fig. 7 (a) Linear plot of log $i(V)$ *vs.* log scan rate (v), (b) comparison of the contributions of surface capacitive and diffusion processes, (c) percentage of the capacitive map of the CV curve at 2 mV s^{-1} and (d) percentage of the capacitive map of the CV curve at 40 mV s^{-1}.

Dunn's method was employed to study the dependence of the CV curves on the sweep speeds to quantify the contributions of diffusion-controlled processes and surface capacitive effects. Eqn (5) was used to calculate the ratio of two contributions as follows.[79]

$$i(V) = k_1 v + k_2 v^{1/2} \quad (7)$$

where the constants k_1 and k_2 represent the slope and intercept of the plot of $i(V)/v^{1/2}$ against $v^{1/2}$, i and v stand for current and scan rate, respectively. The current contributions from capacitive behavior and diffusion-controlled behavior are shown by the values of $k_1 v$ and $k_2 v^{1/2}$, respectively.

Fig. 7(b) displays eqn (5) at a scan rate of 2 mV s^{-1}, and it was found that surface capacitive behaviour contributes approximately 14% to the overall capacity. In contrast, at a scan rate of 40 mV s^{-1}, the capacitive contribution increases to 41%. As the scan rate increases, the capacitive effect also increases significantly due to the fact that electrolyte ions do not have enough time to interact with the electrode to have a redox reaction to be fully realized. Consequently, the diffusion-controlled faradaic intercalation contribution decreases from 86% at 2 mV s^{-1} to 59% at 40 mV s^{-1}, as illustrated in Fig. 7(c and d). This confirms the previously discussed faradaic behavior of ZIF-67 : Ni (1 : 2).

3.2.3 Two-electrode configuration (full-cell). To further confirm the practical usefulness of the optimized electrode, an asymmetric supercapacitor device with ZIF-67 : Ni (1 : 2) as the positive electrode, because of its electrochemical dominance over other composites, including pristine ZIF-67, and AC derived from peanut shell (PAC)[11] as the negative electrode was assembled (Fig. 8(a)). The asymmetric device was assembled with a charge balance equivalent to masses of 3.5 mg for the positive electrode and 1 mg for the negative electrode, calculated from mass balancing eqn (2). The electrochemical performance of the ZIF-67 : Ni (1 : 2)//AC asymmetric cell was evaluated in 6 M KOH aqueous electrolyte. Fig. 8(b) illustrates the CV curves of the negative electrode (PAC) and positive electrode (ZIF-67 : Ni (1 : 2)) reaching their potential window limits in the three electrode configurations. The CVs of the PAC electrode displayed a typical electrical double-layer capacitor with a rectangular shape, whereas ZIF-67 : Ni (1 : 2) shows a faradaic feature at 20 mV s^{-1}. Fig. 8(c) displays the CVs of the assembled ZIF-67 : Ni (1 : 2)//AC device at a scan rate varying from 10 mV s^{-1} to 500 mV s^{-1}. These curves show a merge of the combined features of AC and ZIF-67 : Ni (1 : 2). The CVs show expected redox peaks and uneven rectangular shapes at all evaluated scan rates. The presence of these redox peaks suggests that the ZIF-67 : Ni (1 : 2) electrode dominates in the ZIF-67 : Ni (1 : 2)//AC device. The shapes of CV curves remain

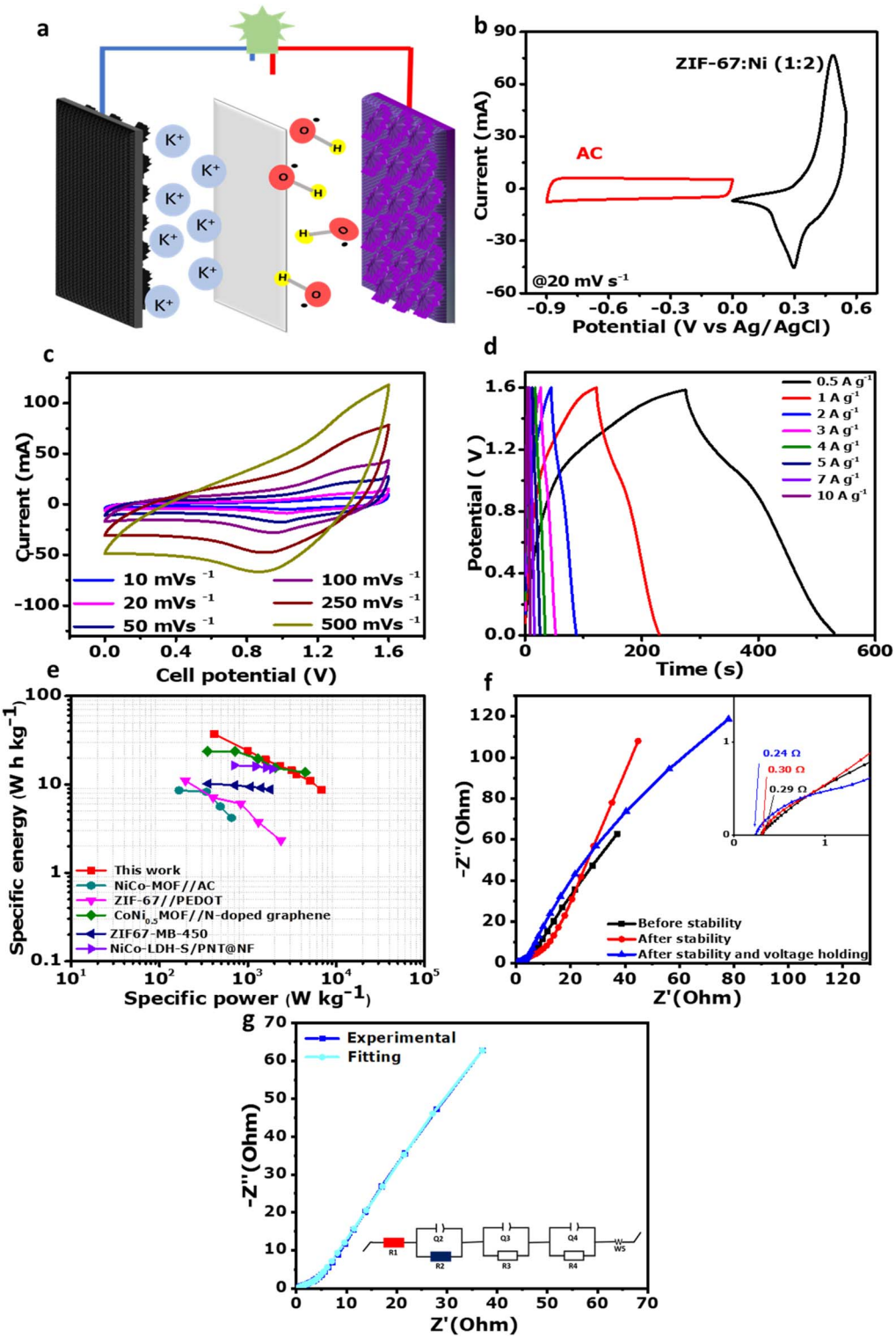

Fig. 8 Electrochemical performance of ZIF-67 : Ni (1 : 2)//AC supercapacitor: (a) schematic diagram of the fabricated supercapacitor device, (b) CV curves comparing ZIF-67 : Ni (1 : 2) and PAC electrodes at 20 mV s^{-1}, (c) CV curves at various scan rates, (d) galvanostatic charge–discharge (GCD) curves at different current densities, (e) Ragone plot showing energy and power density relationship, (f) Nyquist plot with inset displaying the high-frequency region, and (g) equivalent circuit model used for EIS data fitting prior to cycling stability testing.

nearly unchanged with the increase in scan rates, suggesting that the device demonstrates good electrochemical reversibility. Fig. 8(d) shows the GCD patterns of the ZIF-67 : Ni (1 : 2)//AC asymmetric device at various specific currents. The GCD patterns indicate nearly symmetrical charge–discharge at all evaluated specific currents, which indicate a good stability of

this device at a voltage of 1.6 V. The device rate capability (29.14%) was evaluated using specific capacities *versus* specific current plot illustrated in Fig. S8(a). The results confirmed the advantage of incorporating nickel for improving the electrochemical performance of the electrode materials.

Furthermore, these results also indicate better performance of our device as compared with the MOF-based supercapacitor devices that have been recently published in the literature, such as porous ZIF-67/PEDOT//AC (11 W h kg^{-1} at 200 W kg^{-1}),[40] and $CoNi_{0.5}$-MOF//N-doped graphene (23.44 W h kg^{-1} at 350 W kg^{-1}),[55] among others, also shown in Table 3.

Cycling performance, which is evaluated by GCD measurements at 10 A g^{-1} specific current, is shown in Fig. S7(b). The capacity retention and coulombic efficiency of the ZIF-67 : Ni (1 : 2)//AC device are around 61.7% and 99.8% after 10 000 GCD test cycles, suggesting potential practical applications of the device. Fig. 8(f) presents the Nyquist plots of the ZIF-67 : Ni (1 : 2)//AC cell before ($R_s = 0.29\ \Omega$), after the stability test ($R_s = 0.30\ \Omega$), and after voltage holding ($R_s = 0.24\ \Omega$), which displayed a significant increase in the diffusion length, respectively. The minimal difference in R_s values indicates excellent electrode stability, as shown in the Nyquist plots (Fig. 8(g) and S8(d)) for the ZIF-67 : Ni (1 : 2)//AC supercapacitor before cycling, after cycling, and during voltage holding tests. The fitting model was generated using ZFIT/EC-Lab version 11.50 using randomize + simplex fitting algorithms. This fitting, as obtained at an optimized minimized error, which are chi-squared (χ^2) and $\chi/\sqrt{N}$. The $\chi/\sqrt{N}$, is a normalized expression of χ^2, where N is the number of data points, whose value is independent of the number of points. After voltage holding, the circuits are identical except for an additional Warburg response, which confirms that the electrode maintains excellent conductivity and interfacial stability even after prolonged testing.[83] The EIS curve after the cycle displays a slight increase in internal resistance after stability, but a decline after 120 h of floating time Fig. S8(d). During voltage holding Fig. S8(c), the specific capacity initially increases from 12.6 mA h g^{-1} to 14.4 mA h g^{-1} within the first 20 hours. Between 30 and 60 hours, there is another increase in specific capacity from 13.5 to 16.7 mA h g^{-1}, which then stabilizes until 120 hours. As observed in the literature,[84] prolonged device operation at high operating potentials improves the discharge time and enhances the specific capacity of the device due to the redox activity within the open pores of the materials. This indicates the electrolyte ions were able to diffuse and access the electrode material further. The Bode curve of the asymmetric device is shown in Fig. S8(e), which displays the plot of phase angle *vs.* frequency. At low frequencies, the phase angle of the cell is −59°, which is normally seen for both faradaic and capacitive characteristics.[83]

The variance of imaginary capacity $C''(\omega)$ and real capacity $C'(\omega)$ as a function of frequency is shown in Fig. S8(f); these capacities are calculated from the equations (eqn S(1)–S(3)). The relaxation time τ is defined as $1/2\pi f_0$, representing the minimum time required to charge the device.[78] The small value ($\tau = 3.9$ s) shows that the charging is very fast for this asymmetric device.

4. Conclusion

In conclusion, we have explored a facile room temperature solution-phase synthesis method to design and optimize nickel-incorporated ZIF-67 MOF for supercapacitor application. By optimizing the amount of Ni^{2+} ions into ZIF-67, the best sample was ZIF-67 : Ni (1 : 2). The ZIF-67 : Ni (1 : 2) hybrid-MOF electrode, in particular, showed a high specific capacity of 161.2 mA h g^{-1} at 1 A g^{-1} as compared to other concentrations, which are (1 : 1) and (1 : 4) in three electrode tests. Additionally, the ZIF-67 : Ni (1 : 2) MOF exhibits good cycling stability, retaining 74.6% of its specific capacity after 5000 cycles in a three-electrode cell configuration. More significantly, the assembled asymmetric device of ZIF-67 : Ni (1 : 2)//AC demonstrates an outstanding specific energy of 36.97 W h kg^{-1} and specific power of 416.3 W kg^{-1} at a specific current of 0.5 A g^{-1}. After 10 000 cycles, the device displayed a great coulombic efficiency of 99.8%. The enhanced electrochemical performances of ZIF-67 : Ni (1 : 2) are primarily due to its unique structure and the combined action of Ni clusters and ZIF-67, as demonstrated by the electrochemical characterization. The stability of MOF materials is increased by Ni clusters being enclosed in the pores of the ZIF-67 framework. In addition to offering charge transport, the ZIF-67 : Ni (1 : 2) smaller

Table 3 Performance comparison of ZIF-67 : Ni (1 : 2)//AC in two electrodes with relevant MOF composites in the literature[a]

Electrode	Cell potential (V)	Electrolyte	Energy density (W h kg^{-1})	Power density (W kg^{-1})	Ref.
ZIF-67/PEDOT//AC	1.6	1 M H_2SO_4	11	200	40
NiCo-MOF NSHS//AC	1.5	3 M KOH	20.94	750.84	80
Ni/Co-MOF-74-5//AC	1.5	6 M KOH	24.4	784.2	81
ZIF67 MB-450	1.4	3 M KOH	7.15	250	27
$CoNi_{0.5}$-MOF//N-doped graphene	1.4	2 M KOH	23.44	350	55
Ni,Co-MOF/NF//PG/NF	1.6	3 M KOH	32.4	301.5	82
Co_2-Ni-MOF//AC HSC	1.5	6 M KOH	25.92	375	70
ZIF-67//AC	**1.6**	**6 M KOH**	**7.5**	**546.9**	**This work**
ZIF-67 : Ni (1 : 2)//AC	**1.6**	**6 M KOH**	**36.9**	**416.3**	**This work**

[a] ZIF-67 : Ni (1 : 2)//AC is notable for its ability to reach a maximum energy density of 36.9 W h kg^{-1} and a power density of 416.3 W kg^{-1} at the lowest specific current of 0.5 A g^{-1}.

microsphere structure also demonstrated outstanding electrochemical performance by providing more active sites for electrode reactions. The synthesis method employed in this work displays a good prospect for energy storage applications.

Author contributions

Ndeye Fatou Diop, Kabir Otun and Ncholu Manyala conceived the idea. Ndeye Fatou Diop drafted the concept by synthesizing, characterising and writing the manuscript. Kabir Opeyemi Otun, Souleymane Thior, Vusani Muswa Maphiri, Vianney Ngoyi Kitenge, Samba Sarr, Ndeye Fatou Sylla read, reviewed and edited the manuscript. Xiang Wenqiang, Mohamed Chaker performed the XPS analysis in Canada. Balla Diop Ngom and Ncholu Manyala as supervisors reviewed and edited the manuscript. All authors examined the results, read the manuscript and unanimously agreed with its content.

Conflicts of interest

There are no conflicts to declare.

Data availability

All the data used for this work are within the article and supporting documents. Further inquiries can be directed to the corresponding author.

Supplementary information: Additional electrochemical and characterization data. See DOI: **https://doi.org/10.1039/d5ra05741h**.

Acknowledgements

This work was supported by the National Research Foundation (NRF) SARChI Chair in Nanomaterials for Energy Storage and Water Purification Applications (Grant No. RNESW240307208354). All the ideas, findings, recommendations, and conclusions in this work are of the author(s); hence, NRF does not take any liability in this regard. Ndeye Fatou Diop is grateful to the University of Pretoria for the bursary through the UP Doctoral Research Bursary.

References

1 H. Xing, G. Long, J. Zheng, H. Zhao, Y. Zong, X. Li, Y. Wang, X. Zhu, M. Zhang and X. Zheng, *Electrochim. Acta*, 2020, **337**, 135817.
2 N. F. Sylla, N. M. Ndiaye, B. D. Ngom, B. K. Mutuma, D. Momodu, M. Chaker and N. Manyala, *J. Colloid Interface Sci.*, 2020, **569**, 332–345.
3 K. O. Oyedotun, K. Makgopa, T. T. Nkambule, M. K. Mathe, K. O. Otun and B. B. Mamba, *Polymers*, 2024, **16**, 1859.
4 K. O. Otun, S. Zong, D. Hildebrandt and X. Liu, *J. Phys. Chem. Solids*, 2022, **167**, 110779.
5 T. S. Mathis, N. Kurra, X. Wang, D. Pinto, P. Simon and Y. Gogotsi, *Adv. Energy Mater.*, 2019, **9**(39), 1902007.
6 M. Harilal, B. Vidyadharan, I. I. Misnon, G. M. Anilkumar, A. Lowe, J. Ismail, M. M. Yusoff and R. Jose, *ACS Appl. Mater. Interfaces*, 2017, **9**, 10730–10742.
7 G. Rutavi, D. J. Tarimo, V. M. Maphiri, V. N. Kitenge and N. Manyala, *J. Energy Storage*, 2023, **58**, 106442.
8 J. Zhao and A. F. Burke, *J. Energy Chem.*, 2021, **59**, 276–291.
9 Y. Chen, X. Zhang, C. Xu and H. Xu, *Electrochim. Acta*, 2019, **309**, 424–431.
10 S. Sarr, D. T. Bakhoum, N. F. Sylla, N. M. Ndiaye, D. J. Tarimo, V. M. Maphiri, B. D. Ngom and N. Manyala, *New J. Chem.*, 2024, **48**, 13492–13505.
11 N. F. Sylla, N. M. Ndiaye, B. D. Ngom, D. Momodu, M. J. Madito, B. K. Mutuma and N. Manyala, *Sci. Rep.*, 2019, **9**, 1–15.
12 S. Saini, P. Chand and A. Joshi, *J. Energy Storage*, 2021, **39**, 102646.
13 V. N. Kitenge, D. J. Tarimo, K. O. Oyedotun, G. Rutavi and N. Manyala, *J. Energy Storage*, 2022, **56**, 105876.
14 B. D. Ngom, N. M. Ndiaye, N. F. Sylla, B. K. Mutuma and N. Manyala, *Sustainable Energy Fuels*, 2020, **4**, 4814–4830.
15 D. Wei, J. Wang, J. Yin and L. Xu, *J. Alloys Compd.*, 2023, **969**, 172364.
16 Y. Du, R. Liang, J. Wu, Y. Ye, S. Chen, J. Yuan, J. Chen and P. Xiao, *RSC Adv.*, 2022, **12**, 5910–5918.
17 R. Baweja, M. Verma, S. Gautam, S. Upreti and N. Goyal, *RSC Adv.*, 2024, **14**, 17855–17865.
18 S. Gautam, S. Rialach, S. Paul and N. Goyal, *R. Soc. Chem.*, 2024, **14**, 14311–14339.
19 F. Ran, M. Hu, S. Deng, K. Wang, W. Sun, H. Peng and J. Liu, *R. Soc. Chem.*, 2024, **14**, 11482–11512.
20 S. Zhao, L. Zeng, G. Cheng, L. Yu and H. Zeng, *Chin. Chem. Lett.*, 2019, **30**, 605–609.
21 K. O. Otun, N. F. Diop, O. Fasakin, R. A. M. Adam, G. Rutavi and N. Manyala, *RSC Adv.*, 2025, **15**, 4120–4136.
22 Z. Wang, Y. Zhong, C. Wei, L. Jiang and H. Liu, *J. Electrochem. Soc.*, 2022, **169**, 010516.
23 J. Cao, Y. Li, L. Wang, Y. Qiao, J. Li, L. Zhu, S. Zhang, X. Yan and H. Xie, *J. Alloys Compd.*, 2023, **93**, 168262.
24 S. Sundriyal, H. Kaur, S. K. Bhardwaj, S. Mishra, K. H. Kim and A. Deep, *Coord. Chem. Rev.*, 2018, **369**, 15–38.
25 C. Xia, T. Ren, R. Darabi, M. Shabani-Nooshabadi, J. Jaromír Klemeš, C. Karaman, F. Karimi, Y. Wu, H. Kamyab, Y. Vasseghian and S. Chelliapan, *Energy*, 2023, **270**, 126914.
26 R. Zhao, H. Xie, L. Chang, X. Zhang, X. Zhu, X. Tong, T. Wang, Y. Luo, P. Wei, Z. Wang and X. Sun, *EnergyChem*, 2019, **1**, 100011.
27 T. R. Kuo, H. T. Draviana, C. S. Hsu, R. J. Chung, M. W. Chen, S. C. Wang, P. Y. Lee, S. Yougbaré, L. Y. Lin and Y. F. Wu, *J. Energy Storage*, 2023, **68**, 107831.
28 N. Raza, T. Kumar, V. Singh and K. H. Kim, *Coord. Chem. Rev.*, 2021, **430**, 213660.
29 C. Wang, M. Zhou, H. Cao, H. Lin and S. Han, *Mol. Syst. Des. Eng.*, 2024, **9**, 243–253.
30 X. Shang, H. Mei, Z. Li, C. Dong, Z. Wang and B. Xu, *New J. Chem.*, 2021, **45**, 13979–13985.
31 V. Virender, V. Pandey, G. Singh, P. K. Sharma, P. Bhatia, A. A. Solovev and B. Mohan, *Top. Curr. Chem.*, 2024, **383**(1), 3.

32 Y. F. Wu, Y. C. Hsiao, C. H. Liao, C. S. Hsu, S. Yougbaré and L. Y. Lin, *J. Colloid Interface Sci.*, 2022, **628**, 540–552.
33 A. H. A. Rahim and S. R. Majid, *J. Appl. Electrochem.*, 2023, **53**, 1727–1737.
34 Q. Pan, M. Yang, F. Song, Z. Xiong and X. He, *Vacuum*, 2024, **225**, 113203.
35 H. Shooshtari Gugtapeh and M. Rezaei, *ACS Appl. Mater. Interfaces*, 2023, **15**, 34682–34697.
36 R. Zhang, T. Zhou, L. Wang and T. Zhang, *ACS Appl. Mater. Interfaces*, 2018, **10**, 9765–9773.
37 M. P. Dojčinović, I. Stojković Simatović and M. V. Nikolić, *Materials*, 2024, **17**(6), 1292.
38 G. A. Giffin, *Nature Research*, 2022, **13**(1), 5250.
39 S. Wang, X. Zhang, Q. Xiang, S. Zhou, J. Zheng, R. Yan and G. Gao, *New J. Chem.*, 2023, **47**, 13297–13302.
40 V. Shrivastav, S. Sundriyal, A. Kaur, U. K. Tiwari, S. Mishra and A. Deep, *J. Alloys Compd.*, 2020, **843**, 155992.
41 J. T. Kloprogge and R. L. Frost, *J. Solid State Chem.*, 1999, **146**, 506–515.
42 A. Ju, R. Xu, Y. Zhang, S. Feng, C. Chen and J. Liao, *Int. J. Electrochem. Sci.*, 2021, **16**, 210422.
43 P. Thangasamy, S. Shanmuganathan and V. Subramanian, *Nanoscale Adv.*, 2020, **2**, 2073–2079.
44 W. R. Yan, Y. Xue, M. C. Liu, X. Qiao, C. Y. Jing, Y. Yu, X. C. Yan, J. Z. Wei, H. Dong and F. M. Zhang, *CrystEngComm*, 2024, **26**, 3185–3193.
45 S. Wang, C. Xiang, Z. Xiao, F. Xu, L. Sun and Y. Zou, *J. Energy Storage*, 2023, **59**, 106555.
46 S. Kaushik, P. Chand and S. Sharma, *Electrochim. Acta*, 2024, **497**, 144565.
47 A. G. Dymerska, B. Środa, B. Zielińska and E. Mijowska, *Mater. Des.*, 2023, **226**, 111637.
48 J. J. Zhou, W. Ji, L. Xu, Y. Yang, W. Wang, H. Ding, X. Xu, W. Wang, P. Zhang, Z. Hua and L. Chen, *Chem. Eng. J.*, 2022, **428**, 132123.
49 S. Sun, M. Huang, P. Wang and M. Lu, *J. Electrochem. Soc.*, 2019, **166**, A1799–A1805.
50 V. M. Maphiri, L. T. Melato, M. R. Mhlongo, T. T. Hlatshwayo, T. E. Motaung, L. F. Koao and S. V. Motloung, *J. Rare Earths*, 2023, **41**, 358–364.
51 C. Cheng, Y. Zou, F. Xu, C. Xiang and L. Sun, *Nanomaterials*, 2023, **13**, 581.
52 C. Wu, D. Xie, Y. Mei, Z. Xiu, K. M. Poduska, D. Li, B. Xu and D. Sun, *Phys. Chem. Chem. Phys.*, 2019, **21**, 17571–17577.
53 A. Elsonbaty, A. M. Elshaer, M. Harb, M. Soliman, S. Ebrahim and A. Eltahan, *Electrochim. Acta*, 2021, **368**, 137577.
54 Y. Chen, N. Wang, W. Hu and S. Komarneni, *J. Porous Mater.*, 2019, **26**, 921–929.
55 W. Zhang, X. Guo, Y. Wang, Y. Zheng, J. Zhao, H. Xie, Z. Zhang and Y. Zhao, *Energy Fuels*, 2022, **36**, 1716–1725.
56 X. Qing, C. Zhang, Y. Wang, S. Wang, C. Xiang, F. Xu, L. Sun and Y. Zou, *J. Alloys Compd.*, 2024, **1005**, 176107.
57 X. Luo, M. Zhang, Y. Hu, Y. Xu, H. Zhou, Z. Xu, Y. Hao, S. Chen, S. Chen, Y. Luo and Y. Lin, *Science*, 2024, **385**(6709), 647–651.
58 C. Yan, F. Guo, H. Cai, L. Liu, Y. Li, Y. Kang and Z. Dou, *Coatings*, 2025, **15**, 197.
59 Y. Yan, M. Huang, Y. Wang, D. He and J. He, *Heliyon*, 2024, **10**, 25586.
60 Y. Chi, W. Yang, Y. Xing, Y. Li, H. Pang and Q. Xu, *Nanoscale*, 2020, **12**, 10685–10692.
61 J. Hong, S. J. Park and S. Kim, *Electrochim. Acta*, 2019, **311**, 62–71.
62 A. M. Kale, R. Manikandan, C. Justin Raj, A. Dennyson Savariraj, C. Voz and B. C. Kim, *Mater Today Energy*, 2021, **21**, 100736.
63 G. Meng, F. Zhan, J. She, J. Xie, Q. Zheng, Y. Cheng and Z. Yin, *Nanoscale*, 2023, **15**, 15994–16001.
64 M. Huang, K. Mi, J. Zhang, H. Liu, T. Yu, A. Yuan, Q. Kong and S. Xiong, *J. Mater. Chem. A*, 2017, **5**, 266–274.
65 Z. Yang, Y. W. Chen, Y. F. Jin, Z. Jin, H. S. Xie, X. S. Cong and D. G. Teng, *ACS Omega*, 2024, **9**, 11356–11365.
66 G. Yang, J. Liu, M. Zhou, J. Bai and X. Bo, *ACS Sustain. Chem. Eng.*, 2020, **8**, 11947–11955.
67 Z. A. Alothman, *Materials*, 2012, **5**(12), 2874–2902.
68 Z. Wang, X. Jiang, M. Pan and Y. Shi, *Minerals*, 2020, **10**(4), 377.
69 X. Hang, J. Zhao, Y. Xue, R. Yang and H. Pang, *J. Colloid Interface Sci.*, 2022, **628**, 389–396.
70 J. Wang, Q. Zhong, Y. Xiong, D. Cheng, Y. Zeng and Y. Bu, *Appl. Surf. Sci.*, 2019, **483**, 1158–1165.
71 F. Ma, S. Jin, Y. Li, Y. Feng, Y. Tong and B. C. Ye, *J. Electroanal. Chem.*, 2022, **904**, 115932.
72 M. Yao, N. Wang, W. Hu and S. Komarneni, *Appl. Catal., B*, 2018, **233**, 226–233.
73 C. Li, L. Sha, K. Yang, F. Kong, P. Li, Y. Tao, X. Zhao and H. Chen, *Front. Chem.*, 2022, **10**, 1–11.
74 M. Diop, B. M. Ndiaye, S. Dieng, B. D. Ngom and M. Chaker, *RSC Adv.*, 2024, **14**, 5782–5796.
75 H. Guo, M. Xu, L. Yue, Q. Li, N. Wu, M. Wang, X. Wang and W. Yang, *Adv. Mater. Interfaces*, 2019, **6**, 1901571.
76 D. Zheng, H. Wen, X. Sun, X. Guan, J. Zhang, W. Tian, H. Feng, H. Wang and Y. Yao, *Chem.–Eur. J.*, 2020, **26**, 17149–17155.
77 H. Liu, X. Liu, S. Wang, H. K. Liu and L. Li, *Energy Storage Mater.*, 2020, **28**, 122–145.
78 Y. Y. Kannangara, S. Karunarathne, W. P. S. L. Wijesinghe, C. Sandaruwan, C. R. Ratwani, A. R. Kamali and A. M. Abdelkader, *J. Energy Storage*, 2024, **84**, 110717.
79 Y. Jiang and J. Liu, *Energy Storage Mater.*, 2019, **2**(1), 30–37.
80 J. Sun, X. Yu, S. Zhao, H. Chen, K. Tao and L. Han, *Inorg. Chem.*, 2020, **59**, 11385–11395.
81 S. Guo, X. Xu, J. Liu, Q. Zhang and H. Wang, *J. Electrochem. Soc.*, 2020, **167**, 020539.
82 S. Salehi, M. H. Ehsani and M. Aghazadeh, *J. Alloys Compd.*, 2023, **940**, 168885.
83 G. Rutavi, D. J. Tarimo, V. M. Maphiri, V. N. Kitenge and N. Manyala, *J. Alloys Compd.*, 2022, **929**, 167216.
84 O. Fasakin, J. K. Dangbegnon, D. Y. Momodu, M. J. Madito, K. O. Oyedotun, M. A. Eleruja and N. Manyala, *Electrochim. Acta*, 2018, **262**, 187–196.